

Exploiting negative differential resistance in monolayer graphene FETs for high voltage gains

Roberto Grassi, Antonio Gnudi, *Member, IEEE*, Valerio Di Lecce, Elena Gnani, *Member, IEEE*, Susanna Reggiani, *Member, IEEE*, and Giorgio Bacarani, *Fellow, IEEE*

Abstract—Through self-consistent quantum transport simulations, we evaluate the RF performance of monolayer graphene FETs in the bias region of negative output differential resistance. We show that, compared to the region of quasi-saturation, a voltage gain larger than 10 can be obtained, at the cost of a decrease in the maximum oscillation frequency of about a factor of 1.5–3 and the need for a careful circuit stabilization.

Index Terms—Graphene FET, negative differential resistance, terahertz operation, voltage amplifier.

I. INTRODUCTION

GRAPHENE has been suggested as a promising material for analog and radio-frequency (RF) applications due to its exceptional electrical properties. In particular, the high mobility and large group velocity can translate to a high device transconductance g_m and high cut-off frequency f_T , and there is no need for a band gap to switch off the device as in digital applications [1]. Fabricated graphene field-effect transistors (GFETs) exhibiting f_T of hundreds of gigahertz have already been reported [2]–[5], together with the first applications [6]–[9]. However, challenges still remain. Particularly in short-channel devices, where velocity saturation does not occur, the lack of a band gap leads to poor current saturation (i.e., pronounced drain conductance g_d), which negatively affects the device performance as an amplifier. This is especially true at low frequency, where the ability to amplify signals is expressed by the intrinsic voltage gain g_m/g_d , which is limited to only few units in monolayer GFETs [8]–[11], with a record value of 5.3 for channel lengths of the order of 1 μm . While voltage gain is not strictly necessary at high frequency, a large g_d also contributes to degrade to some extent the maximum oscillation frequency f_{max} , which is the maximum frequency at which power gain can be obtained, and, in many applications, represents a more important figure of merit than f_T [12].

To address the above issues, the use of bilayer graphene, where a band-gap can be introduced through a vertical electric field, has been suggested and values of g_m/g_d as high as 35 have been experimentally demonstrated [13], [14]. In this paper, as an alternative approach, we study whether the RF performance of monolayer GFETs, in particular the voltage

This work has been supported by the EU project GRADE 317839. The authors acknowledge the CINECA Award N. HP10CNHR0P, 2012 for the availability of high performance computing resources and support.

The authors are with the E. De Castro Advanced Research Center on Electronic Systems (ARCES), University of Bologna, 40136 Bologna, Italy (e-mail: rgrassi@arces.unibo.it).

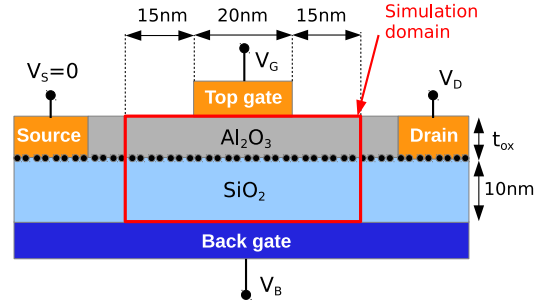


Fig. 1. Longitudinal cross-section of the device under study. The graphene layer is indicated by the black dots. The function of the back-gate is to dope electrostatically the graphene underlap regions between the top gate and the source and drain contacts. The source voltage is taken as the reference.

gain, can be improved by choosing the bias point in the region of negative differential drain resistance (NDR), i.e., of negative g_d . Such NDR has been observed experimentally in long-channel devices [15], [16] and predicted by numerical simulations for short-channel lengths as well [17]–[22], but an analysis of the device small-signal behavior in the NDR region has not been reported yet. Obviously, a device with negative g_d cannot be used as amplifier with a high-impedance load, since the resulting circuit is unstable. However, if the load impedance $1/G_L$ is sufficiently low, the parallel of g_d and G_L can be made positive and, in principle, smaller than the achievable values of g_d in the standard bias region of quasi-saturation, thus potentially resulting in a higher voltage gain.

The objective of the paper is to numerically investigate the feasibility of the above idea. Steady-state simulations are performed to compute the dc I – V and Q – V characteristics of the device, which allow the extraction of the parameters of a small-signal equivalent circuit and, ultimately, of the analog and RF figures of merit. The device structure, simulation model, and small-signal model are described in Section II. The I – V characteristics are presented in Section III, where the connection between g_m and the underlying device physics is also clarified. The circuit stability of the device in the common-source configuration, for a bias point in the NDR region, is analyzed in detail in Section IV. RF performance is discussed in Section V, followed by conclusions in Section VI.

II. DEVICE STRUCTURE AND MODEL

We consider the dual-gate device structure represented in Fig. 1, which is similar to the experimental one in [4], although

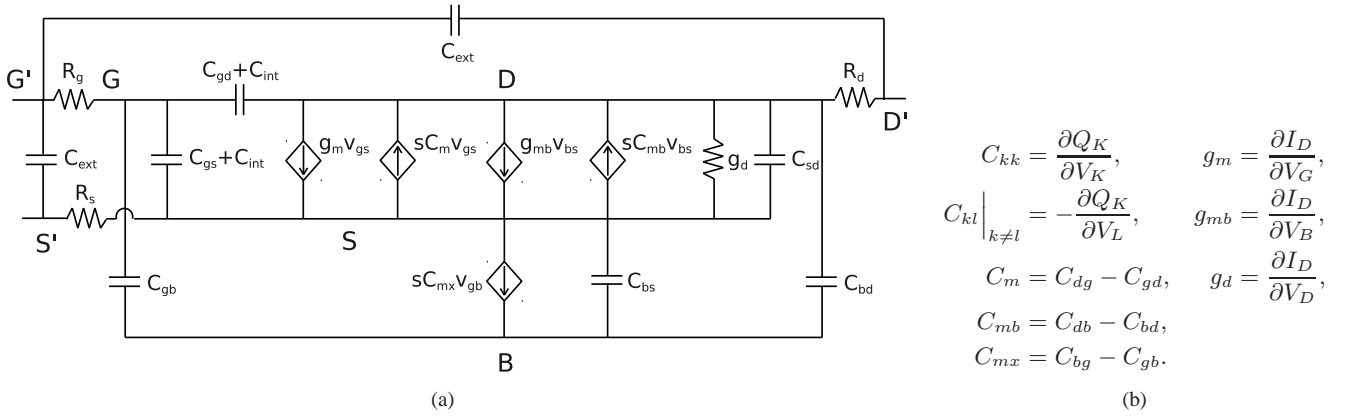


Fig. 2. (a) Small-signal equivalent circuit. Here, the unprimed/primed symbols indicate the intrinsic/extrinsic device terminals. (b) Definition of the intrinsic parameters where $k, l \in \{g, d, s, b\}$ [23]. Q_G and Q_B are the charges on the top gate and back gate, respectively; Q_S and Q_D are the charges on the graphene layer attributed to the source and drain terminals, respectively.

more aggressively scaled. A gate length L_g of 20 nm is assumed. The top dielectric layer is Al_2O_3 ($\kappa = 9.5$), while the back dielectric is silicon oxide with thickness of 10 nm. The top oxide thickness t_{ox} and the back-gate-to-source voltage V_{BS} are treated as parameters. Nominal values are: $t_{ox} = 1.2$ nm (effective oxide thickness EOT = 0.5 nm) and $V_{BS} = 9$ V. Contrary to previous simulations of NDR in GFETs, we do not assume metal-doped [19], [20] or chemically-doped [21], [22] source and drain regions, but instead we let the doping of the graphene underlap regions between the top gate and the source and drain contacts be controlled by the back gate. The effective doping corresponding to $V_{BS} = 9$ V is about $1.9 \times 10^{13} \text{ cm}^{-2}$. From a technological point of view, such electrostatic doping technique is easier and more controllable, although the dual gate structure introduces some complications due to the additional wiring and management of the high back-gate voltage.

The simulations are performed using an in-house developed code for GFETs, based on the self-consistent solution of the 2D Poisson equation and the ballistic non-equilibrium Green's function (NEGF) equations [24], with a p_z tight-binding Hamiltonian and a mode-space solution approach. The model is the same as the one in [19] but with a different treatment of the interfaces: the source and drain self-energies are computed with the metal-graphene coupling strength Δ set to zero, and Neumann boundary conditions instead of Dirichlet are used in Poisson's equation at the source and drain ends. Moreover, instead of assuming a finite channel width with periodic boundary conditions as in [19], the device is taken to be infinite in the transverse direction, so that sums over modes are replaced by integrals over the transverse wavevector. The latter are performed by a Gaussian quadrature with 40 k -points.

The small-signal frequency behavior of the device is analyzed through the usual quasi-static approximation, which consists in constructing a small-signal equivalent circuit, whose resistive and capacitive elements are extracted from the dc characteristics of charge and current at the various terminals (Fig. 2). The small-signal circuit model is the same used for silicon MOSFETs [23], with the back gate acting

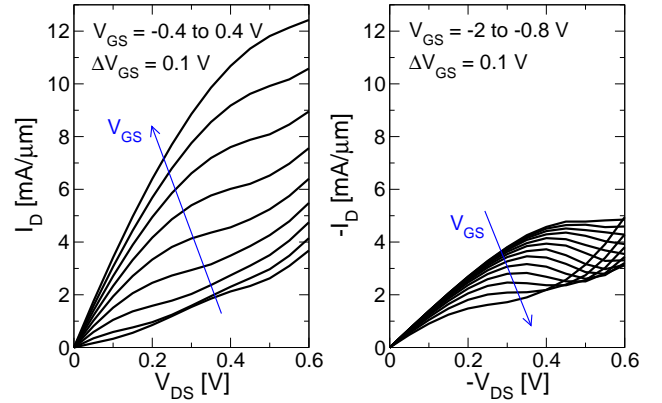


Fig. 3. Output characteristics for $V_{DS} > 0$ and $V_{GS} \geq -0.4$ V, corresponding to an n-type channel (left), and for $V_{DS} < 0$ and $V_{GS} \leq -0.8$ V, corresponding to a p-type channel (right). At high absolute values of drain bias, quasi-saturation is observed in one case while NDR, i.e. negative drain conductance g_d , in the other.

as bulk terminal. The source/drain charge $Q_{S/D}$ is taken equal to the charge contribution relative to injection from source/drain of the ballistic transport model. Other charge-partitioning schemes are possible: the authors of [25] have checked that different choices of Q_S and Q_D (with fixed sum $Q_S + Q_D$) have a negligible impact on their results. Source, drain, and gate contact resistances R_s , R_d , and R_g are included in the model as additional parameters. External parasitic capacitances are modeled according to [26], i.e. through additional capacitive elements between the intrinsic (C_{int}) and extrinsic (C_{ext}) gate-source and gate-drain pairs of terminals. Unless stated otherwise, we set R_g , C_{int} , and C_{ext} to zero.

III. DC CHARACTERISTICS

The output characteristics of the reference device are shown in Fig. 3, in two regions of the V_{DS} - V_{GS} plane: in the first case ($V_{DS} > 0$ and $V_{GS} \geq -0.4$ V) the device operates as an n-type FET and shows quasi-saturation [26], [27]; in the second case ($V_{DS} < 0$ and $V_{GS} \leq -0.8$ V), the device operates as a p-type FET and exhibits NDR, confirming previous simulations

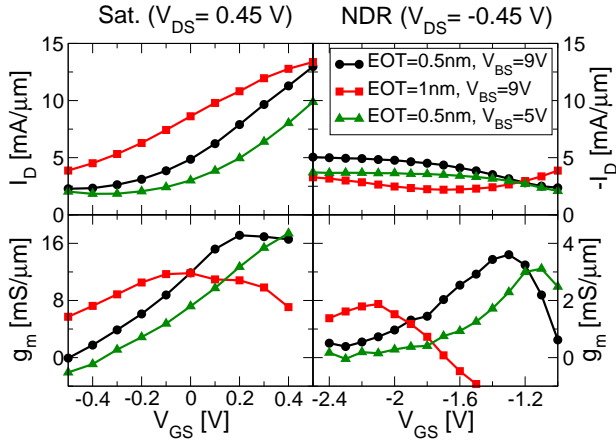


Fig. 4. Transfer characteristics (top) and corresponding transconductance g_m vs. V_{GS} (bottom) at $V_{DS} = 0.45$ V (left) and $V_{DS} = -0.45$ V (right), for the three pairs of EOT and V_{BS} values indicated in the legend.

of GFETs with metal-doped [19], [20] and chemically-doped [21], [22] source and drain regions. The different behavior is due to the formation of either an n-n-n or an n-p-n double junction [20]. The agreement with experiments [15], [16] is only qualitative due to the gap between the conditions considered in the simulation (20-nm channel length and ballistic transport in ideal graphene) and the limitations of the present graphene technology (e.g., contact resistance and interface effects).

NDR is obtained at the cost of lower I_D and transconductance g_m , as is evident from the trans-characteristics and the corresponding g_m vs. V_{GS} plots in Fig. 4. The peak g_m decreases by more than a factor of four. The reason can be ascribed to: (i) reduced transmission due to double band-to-band tunneling across the n-p-n junction [28]; (ii) a transport-mode bottleneck effect induced by the Dirac point at the drain side [20]. Similar asymmetric performance with respect to top gate bias in dual-gated structures is observed in experiments [29], [30]. In Fig. 4, we also show the results obtained by increasing t_{ox} to 2.4 nm (EOT = 1 nm) or by lowering V_{BS} to 5 V (effective doping of 1×10^{13} cm $^{-2}$). As one might expect, a larger EOT leads to significant degradation of the peak g_m , in both bias regions, due to reduced electrostatic control of the top gate on the channel potential. In the bias region corresponding to NDR, a lower V_{BS} also goes in the direction of decreasing the peak g_m , highlighting the importance of a heavy doping of the source and drain regions in this transport regime. Increasing further the drain degeneracy with respect to the case with $V_{BS} = 9$ V would require the use of a high- κ substrate material, for the vertical electric field in the back dielectric is already close to the SiO $_2$ limit of 1 V/nm at $V_{BS} = 9$ V. On the other hand, since a higher κ also implies a larger back gate capacitance, the back oxide thickness (and consequently V_{BS}) should be increased to avoid a counterproductive effect on g_m .

The extracted small-signal parameters for the bias points of peak g_m of the quasi-saturation and NDR regions are provided for reference in Table I. Since the Q - V characteristics (not shown) were found to be affected by numerical noise, we used a Savitsky-Golay filter of order two [31] to compute the

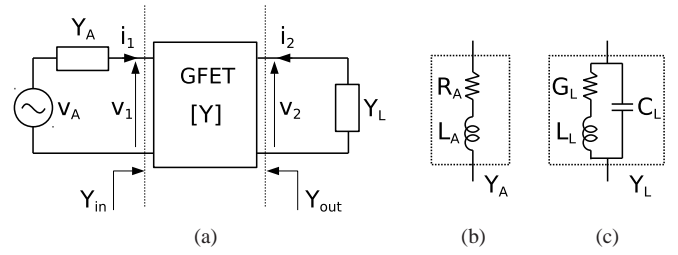


Fig. 5. (a) Representation in terms of Y -parameters of the GFET connected to the source and load networks and symbol definitions. (b-c) Models for the source and load admittances, respectively, which were used to evaluate circuit stability. L_A and L_L represent parasitic inductances.

parameters in Table I, rather than using finite differences as for the g_m plots in Fig. 4.

IV. STABILITY ANALYSIS

In this section, we study the stability of the reference device in the common-source configuration, at $V_{DS} = -0.45$ V and $V_{GS} = -1.3$ V (operating point of peak g_m of the NDR region). We consider a channel width $W = 1$ μ m. From the small-signal circuit of Fig. 2, one can derive the expressions of the Y -parameters of the extrinsic transistor $Y_{11} \dots Y_{22}$, which allow to compute the output and input admittances Y_{out} and Y_{in} as a function of the source and load admittances Y_A and Y_L , respectively (see circuit in Fig. 5(a) for symbol definitions). Regarding the functional dependence of Y_A and Y_L on frequency f , we assume the circuit models in Figs. 5(b)-(c), where L_A and L_L represent series parasitic interconnect inductances.

The stability of an RF amplifier is usually ensured by requiring that both Y_{out} and Y_{in} have a positive real part in the whole frequency range where the amplifier behaves as an active network [32]:

$$\Re\{Y_{out}\} > 0, \quad \Re\{Y_{in}\} > 0. \quad (1)$$

The ‘‘stability circles’’ technique then allows to find on the Smith chart the range of values of Y_A and Y_L for which (1) are satisfied at each frequency. Such approach, however, cannot be applied in the present case, since $\Re\{Y_{out}\}$ is potentially negative at low frequency, where the device is unilateral. The real part of Y_{out} is plotted as a function of frequency in Fig. 6-left for the case of $|Y_A| \equiv \infty$ (short-circuit at the input port) and for values of $R_s = R_d$ from 200 down to 50 $\Omega \cdot \mu$ m, i.e. from typical experimental values down to best achievable ones [33]. The low-frequency value of Y_{out} , given by the output conductance g_{out} of the extrinsic transistor

$$g_{out} = \frac{g_d}{1 + (R_s + R_d)g_d + R_s(g_m + g_{mb})}, \quad (2)$$

is strongly affected by the source and drain contact resistances, as shown in the figure, but is independent of Y_A . We note that stability is still possible if

$$\Re\{Y_{out} + Y_L\} > 0, \quad \Re\{Y_{in} + Y_A\} > 0, \quad (3)$$

which represent less restrictive requirements than (1). Acceptable values of Y_A and Y_L must satisfy both inequalities simultaneously. Let us first start by assuming $|Y_A| \equiv \infty$. We

TABLE I
INTRINSIC SMALL-SIGNAL PARAMETERS AT $V_{DS} = 0.45$ V AND $V_{GS} = 0.2$ V (SAT.), AND AT $V_{DS} = -0.45$ V AND $V_{GS} = -1.3$ V (NDR).

	C_{gd}	C_{gs}	C_{sd}	C_{gb}	C_{bd}	C_{bs}	C_m	C_{mb}	C_{mx}	g_m	g_{mb}	g_d
	[aF/ μm]	[aF/ μm]	[aF/ μm]	[aF/ μm]	[aF/ μm]	[aF/ μm]	[aF/ μm]	[aF/ μm]	[aF/ μm]	[mS/ μm]	[mS/ μm]	[mS/ μm]
Sat.	221	565	273	37	50	84	-306	-9	-3	17.1	0.8	5.0
NDR	-100	985	617	30	42	87	169	8	8	3.8	≈ 0	-6.1

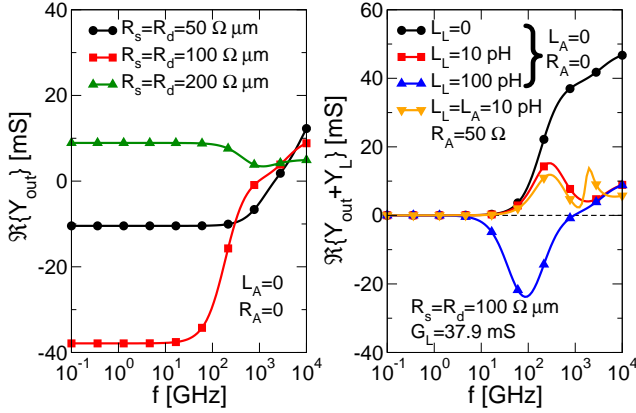


Fig. 6. Stability analysis at the output port for a 1- μm -wide device at $V_{DS} = -0.45$ V and $V_{GS} = -1.3$ V (NDR regime). Left: real part of the output admittance Y_{out} as a function of frequency for different values of source/drain contact resistance, assuming short-circuit at the input port. Right: real part of $Y_{out} + Y_L$ vs. frequency for fixed values of contact resistance and G_L , and for different L_L , L_A , and R_A , as indicated in the legend. Negative values of $\Re\{Y_{out} + Y_L\}$ indicate circuit instability.

consider here a value of contact resistance of $100 \Omega \cdot \mu\text{m}$, for which $g_{out} = -37.9$ mS. To satisfy the first inequality in (3) at low frequency, the negative value of g_{out} must be compensated by a load conductance $G_L > -g_{out}$, as already mentioned in Section I. However, a too large parasitic inductance L_L might cancel the effect of G_L at high frequency, as illustrated by the plot of $\Re\{Y_{out} + Y_L\}$ in Fig. 6-right for different values of L_L (see only the curves with $L_A = R_A = 0$, the other ones being discussed later). We find that L_L must be limited to ≈ 10 pH, an upper bound which should be compatible with an integrated version of the amplifier. Having fixed the values of G_L and L_L this way, we look for values of load capacitance C_L , source resistance R_A , and L_A that allow to satisfy the second inequality in (3). As shown in Fig. 7-left, the real part of Y_{in} is not significantly affected by C_L . Its negative plateau can be compensated by sufficiently low values of R_A and L_A (Fig. 7-right). We find that choosing $R_A = 50 \Omega$, which is the typical characteristic impedance of a transmission line, together with the same upper bound of 10 pH for L_A as for L_L , provides $\Re\{Y_{in} + Y_A\} > 0$. The stability of the circuit is finally demonstrated by checking that the same values of R_A and L_A also give $\Re\{Y_{out} + Y_L\} > 0$ (triangles down in Fig. 6-right). Of course, instead of the procedure outlined here, one could also have tested the circuit stability using the standard pole analysis.

In summary, we have shown that is possible to ensure the stability of the circuit by canceling out the negative real part of Y_{out} and Y_{in} through a proper choice of the load conductance G_L and the source resistance R_A , respectively. The procedure

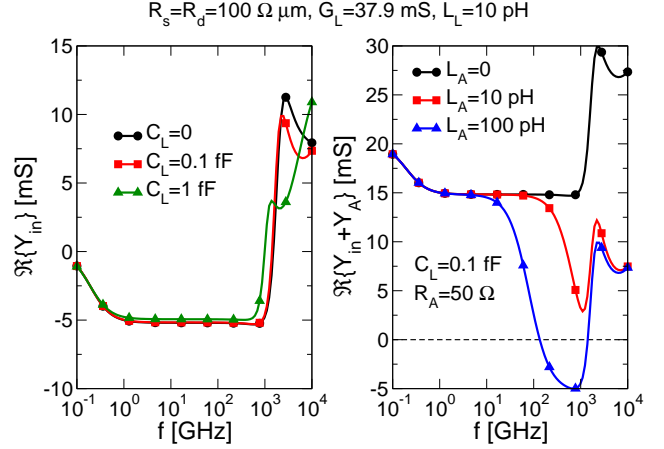


Fig. 7. Stability analysis at the input port for the same device and bias as in Fig. 6, and for $R_s = R_d = 100 \Omega \cdot \mu\text{m}$. G_L and L_L are fixed at values such that $\Re\{Y_{out} + Y_L\}|_{Y_A| \equiv \infty} > 0$ (see Fig. 6-right). Left: real part of the input admittance Y_{in} as a function of frequency for different values of load capacitance C_L . Right: real part of $Y_{in} + Y_A$ vs. frequency for fixed C_L and R_A , and for different L_A . Negative values of $\Re\{Y_{in} + Y_A\}$ indicate circuit instability.

requires: (i) an estimate of the contact resistances and hence of g_{out} ; (ii) small enough parasitic interconnect inductances at the input and output port, or the effect of G_L and R_A is made void at high frequency.

V. ANALOG AND RF METRICS

The following figures of merit are evaluated for the device in the common-source configuration and biased in either the NDR or quasi-saturation region: dc voltage gain $A_{v0} = v_2/v_1|_{f=0}$ with load G_L , cut-off frequency f_T , and maximum oscillation frequency f_{max} . From the small-signal circuit in Fig. 2, a simple expression for A_{v0} can be derived:

$$A_{v0} = -\frac{g_m/g_d}{1 + G_L/g_{out}}, \quad (4)$$

where g_{out} is given by (2). f_T is obtained by extrapolating the low-frequency short-circuit current gain $|H_{21}| = |Y_{21}/Y_{11}|$ to unity at -20 dB/dec, and f_{max} by extrapolating the low-frequency maximum stable gain $\text{MSG} = |Y_{21}/Y_{12}|$ to unity at -10 dB/dec. f_{max} is defined here with reference to MSG rather than Mason's unilateral gain [32], since the latter cannot be defined in the NDR region. In the case of $R_g = C_{int} = C_{ext} = 0$, analytical expressions for f_T and f_{max} can be derived by isolating the $1/s$ terms in the expansion of $Y_{21}(s)/Y_{11}(s)$ and $Y_{21}(s)/Y_{12}(s)$, respectively,

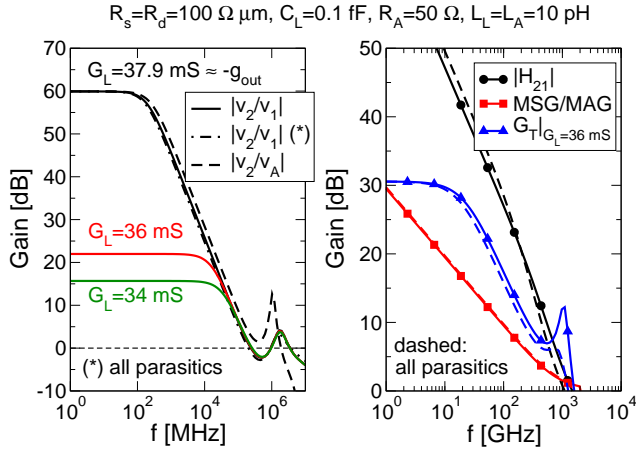


Fig. 8. Plots of voltage gains $|v_2/v_1|$ and $|v_2/v_A|$ vs. frequency (left) and of short-circuit current gain $|H_{21}|$, MSG or MAG (depending on frequency), and transducer gain G_T vs. frequency (right). The dot-dashed curve in (left) and the dashed curves in (right) are obtained with $R_g = 4 \Omega$ and $C_{int} = C_{ext} = 0.1$ fF. Device width and bias are the same as in Fig. 6–7. The other parameters are indicated in the legend.

and by equating their magnitude to unity:

$$f_T = \frac{g_m/(2\pi)}{D}, \quad D = |C_{gg} [1 + (R_s + R_d)g_d + R_s g_{mb}] + C_{gd}(R_s + R_d)g_m + C_{gb}R_s g_m|, \quad (5)$$

$$f_{max} = \frac{g_m/(2\pi)}{|(C_{gs} + C_{gd})R_s g_d + C_{gd} [1 + R_s(g_m + g_{mb})]|}, \quad (6)$$

where the total gate capacitance C_{gg} is related to the circuit elements in Fig. 2 through $C_{gg} = C_{gs} + C_{gd} + C_{gb}$.

Let us start considering the peak- g_m bias point of the NDR region ($V_{DS} = -0.45$ V, $V_{GS} = -1.3$ V) and a value of contact resistance $R_s = R_d = 100 \Omega \cdot \mu\text{m}$. Again, we assume $W = 1 \mu\text{m}$. Fig. 8-left shows the frequency magnitude response of the voltage gain v_2/v_1 for different values of G_L (and fixed values of C_L and L_L). In accordance with (4), the low-frequency value $|A_{v0}|$ is strongly peaked around $G_L = -g_{out} \approx 37.9$ mS. If the difference between G_L and $-g_{out}$ is less than 5%, a voltage gain larger than 10 can be obtained. Furthermore, the larger the gain, the smaller the corresponding bandwidth, resulting in an approximately constant gain-bandwidth product GBW of about 200 GHz. In the same figure, we also plot the frequency response of $|v_2/v_A|$ for $G_L = 37.9$ mS (see legend for values of R_A and L_A), which is found to be almost identical to $|v_2/v_1|$, indicating a minor effect of the source admittance. Even when including the additional parasitics R_g , C_{int} , and C_{ext} , the frequency response does not change significantly. The value of $R_g = 4 \Omega$ considered here has been calculated in a similar way to [25], by assuming a tungsten gate (resistivity of $56 \text{ n}\Omega\cdot\text{m}$) of dimensions $W \times L_g \times t_g = 1 \mu\text{m} \times 20 \text{ nm} \times 60 \text{ nm}$, contacted on both sides [23, Eq. 9.6.2]. The value of $C_{int} = C_{ext} = 0.1$ fF is the same as in [26]. In Fig. 8-right the frequency response of the current gain $|H_{21}|$ and of MSG is reported. For high enough frequencies, where the transistor becomes unconditionally stable, MSG is replaced by the maximum available gain MAG [32] (almost invisible

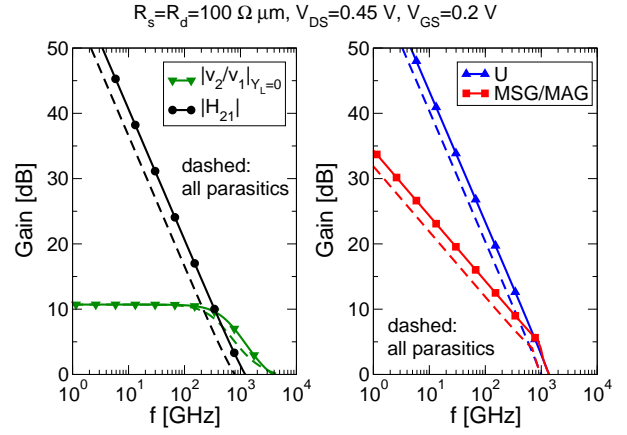


Fig. 9. Plots of voltage gain $|v_2/v_1|$ with open-circuit load and short-circuit current gain $|H_{21}|$ vs. frequency (left), and of MSG or MAG (depending on frequency) and Mason's unilateral gain U vs. frequency (right) for a $1\text{-}\mu\text{m}$ -wide device at $V_{DS} = 0.45$ V and $V_{GS} = 0.2$ V (quasi-saturation regime). The dashed curves are obtained with $R_g = 4 \Omega$ and $C_{int} = C_{ext} = 0.1$ fF. The other parameters are indicated in the legend.

in Fig. 8-right). In the case of $R_g = C_{int} = C_{ext} = 0$, values of $f_T = 2.3$ THz and $f_{max} = 890$ GHz are extracted. For comparison purposes, we also plot the transducer power gain G_T , obtained with source and load parameters (see legend) that ensure the stability of the amplifier. It can be seen that G_T falls off to one at a frequency not too far from f_{max} . Again, the inclusion of additional parasitics has only a limited impact.

Similar plots of voltage gain, current gain, and power gain, but for the peak- g_m bias point of the quasi-saturation region ($V_{DS} = 0.45$ V, $V_{GS} = 0.2$ V), are shown in Fig. 9. For reference, Mason's unilateral gain U is also included. Here, the voltage gain $|v_2/v_1|$ is computed in the open-circuit-load condition, for which $|A_{v0}|$ takes the maximum value $g_m/g_d \approx 3.4$. It can be noted that the voltage gain bandwidth is significantly wider than in the NDR regime. In the case of $R_g = C_{int} = C_{ext} = 0$, values of GBW = 2.1 THz, $f_T = 1.1$ THz and $f_{max} = 2.7$ THz are extracted. The higher f_T in the NDR case can be explained through the beneficial effect of a negative g_d in the denominator of (5), which helps suppress the effect of the source and drain contact resistances. Instead, the lower f_{max} in the NDR regime is caused by the degradation of g_m that was discussed in Section III. Interestingly, the effect of non-zero R_g , C_{int} , and C_{ext} is stronger in the quasi-saturation regime than in the NDR regime. This can be explained at least in the case of $C_{ext} = 0$ and non-zero R_g and C_{int} , for which Eqs. 5–6 are still valid with C_{gs} and C_{gd} replaced by $C_{gs} + C_{int}$ and $C_{gd} + C_{int}$, respectively: since g_d and g_m have opposite sign, they tend to cancel the contributions of the capacitances. The frequency figures of merit extracted in the different cases are reported in Table II. All values reported here for f_{max} are more than an order of magnitude higher than the best values measured in fabricated GFETs (40–70 GHz) [10], [34], a fact that has to be mainly attributed to the ultra-scaled EOT considered in the simulations (0.5 nm rather than 10–20 nm). It is worth noting that the ideal GFETs considered here compete in terms

TABLE II
RF METRICS AT $V_{DS} = 0.45$ V AND $V_{GS} = 0.2$ V (SAT.), AND AT
 $V_{DS} = -0.45$ V AND $V_{GS} = -1.3$ V (NDR).

	$R_g = 0 \Omega$		$R_g = 4 \Omega$	
	$C_{int} = C_{ext} = 0$ fF		$C_{int} = C_{ext} = 0.1$ fF	
	Sat.	NDR	Sat.	NDR
GBW [GHz]	2110	195	1340	172
f_T [GHz]	1080	2280	672	3020
f_{max} [GHz] ^a	2700	891	1540	935
$f_{max,U}$ [GHz] ^b	1470		1040	

^a Unity frequency of MSG. ^b Unity frequency of Mason's unilateral gain.

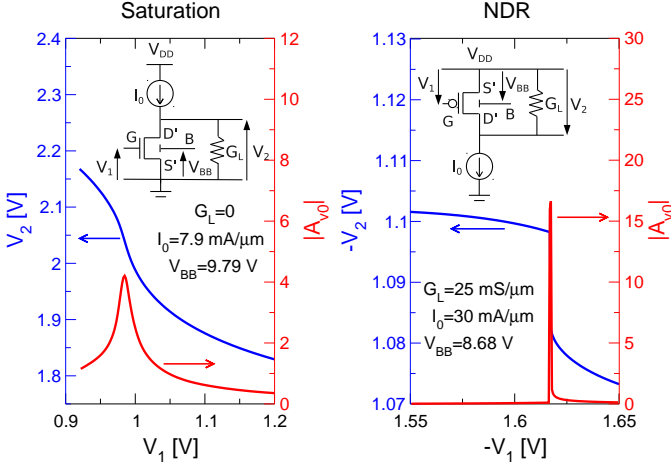


Fig. 10. Voltage transfer characteristics and corresponding voltage gain characteristics for the device biased in the quasi-saturation (left) and NDR region (right), assuming $R_s = R_d = 100 \Omega \cdot \mu\text{m}$. The biasing circuit is shown in the inset of each figure. The discontinuity of $|A_{v0}|$ in (right) is an artifact of the spline interpolation.

of f_{max} with III-V HEMTs [35], despite the lack of current saturation.

Due to the strong dependence of $|A_{v0}|$ on the ratio G_L/g_{out} (Eq. 4), a strong dependence of $|A_{v0}|$ on the operating point is expected too, leading to undesirable non-linearity. In order to check this, we have considered the biasing circuit shown in the inset of Fig. 10-left and of Fig. 10-right, for the quasi-saturation and the NDR case, respectively. The circuit equations have been solved using a spline interpolation of the $I-V$ characteristics with varying V_{BS} . The resulting V_2-V_1 characteristics and the respective voltage gain characteristics are shown in Fig. 10. The higher peak of the voltage gain in the NDR region compared to the quasi-saturation region is obtained at the cost of a much narrower voltage range available to the input signal, which thus limits the use of the device to small-swing signals (< 1 mV) such as those present at the input of a high-speed pre-amplifier stage. While in the quasi-saturation regime the voltage transfer characteristics are similar to those obtained in graphene complimentary inverter amplifiers [36], [37], in the NDR case they resemble the typical characteristics of an inverter amplifier with a high-gain region, thus suggesting negative feedback applications. It should be noted, however, that the output voltage swing is quite limited (< 20 mV).

VI. CONCLUSIONS

In this work, we have investigated the possibility of employing a GFET biased in the region of NDR to achieve higher voltage gains in RF applications. Through a small-signal analysis with parameters extracted from atomistic quantum transport simulations, the stability and RF performance of the transistor in the common-source amplifier configuration have been evaluated. Stability has been found to be a critical issue: compensation of the negative real part of the input and output admittances is required by means of a careful calibration of the source and load networks. Such compensation can be unfeasible if the series parasitic inductance is too large. Voltage gains exceeding the intrinsic gain in the quasi-saturation regime and larger than 10 can actually be achieved. However, this comes at the expenses of a voltage swing available to the input signal smaller than 1 mV and of a reduced bandwidth. Also, f_{max} is found to be smaller than in the quasi-saturation regime as a result of a four-fold decrease of g_m , which is intrinsically related to the device physics responsible for the NDR mechanism.

ACKNOWLEDGMENT

The authors would like to thank Prof. A. Santarelli of University of Bologna and Dr. T. Low of IBM T. J. Watson Research Center for useful discussions.

REFERENCES

- [1] F. Schwierz, "Graphene transistors," *Nature Nanotechnology*, vol. 5, pp. 487–496, 2010.
- [2] L. Liao, Y.-C. Lin, M. Bao, R. Cheng, J. Bai, Y. Liu, Y. Qu, K. L. Wang, Y. Huang, and X. Duan, "High-speed graphene transistors with a self-aligned nanowire gate," *Nature*, vol. 467, no. 7313, pp. 305–308, 2010.
- [3] Y.-M. Lin, C. Dimitrakopoulos, K. A. Jenkins, D. B. Farmer, H.-Y. Chiu, A. Grill, and P. Avouris, "100-GHz Transistors from Wafer-Scale Epitaxial Graphene," *Science*, vol. 327, no. 5966, p. 662, 2010.
- [4] Y. Wu, Y.-M. Lin, A. A. Bol, K. A. Jenkins, F. Xia, D. B. Farmer, Y. Zhu, and P. Avouris, "High-frequency, scaled graphene transistors on diamond-like carbon," *Nature*, vol. 472, no. 7341, pp. 74–78, 2011.
- [5] R. Cheng, J. Bai, L. Liao, H. Zhou, Y. Chen, L. Liu, Y.-C. Lin, S. Jiang, Y. Huang, and X. Duan, "High-frequency self-aligned graphene transistors with transferred gate stacks," *Proceedings of the National Academy of Sciences*, 2012.
- [6] H. Wang, A. Hsu, J. Wu, J. Kong, and T. Palacios, "Graphene-Based Ambipolar RF Mixers," *Electron Device Letters, IEEE*, vol. 31, no. 9, pp. 906–908, 2010.
- [7] Y.-M. Lin, A. Valdes-Garcia, S.-J. Han, D. B. Farmer, I. Meric, Y. Sun, Y. Wu, C. Dimitrakopoulos, A. Grill, P. Avouris, and K. A. Jenkins, "Wafer-scale graphene integrated circuit," *Science*, vol. 332, no. 6035, pp. 1294–1297, 2011.
- [8] S.-J. Han, K. A. Jenkins, A. Valdes Garcia, A. D. Franklin, A. A. Bol, and W. Haensch, "High-frequency graphene voltage amplifier," *Nano Letters*, vol. 11, no. 9, pp. 3690–3693, 2011.
- [9] E. Guerriero, L. Polloni, L. G. Rizzi, M. Bianchi, G. Mondello, and R. Sordan, "Graphene audio voltage amplifier," *Small*, vol. 8, no. 3, pp. 357–361, 2012.
- [10] Y. Wu, K. A. Jenkins, A. Valdes-Garcia, D. B. Farmer, Y. Zhu, A. A. Bol, C. Dimitrakopoulos, W. Zhu, F. Xia, P. Avouris, and Y.-M. Lin, "State-of-the-art graphene high-frequency electronics," *Nano Letters*, vol. 12, no. 6, pp. 3062–3067, 2012.
- [11] L. G. Rizzi, M. Bianchi, A. Behnam, E. Carrion, E. Guerriero, L. Polloni, E. Pop, and R. Sordan, "Cascading wafer-scale integrated graphene complementary inverters under ambient conditions," *Nano Letters*, vol. 12, no. 8, pp. 3948–3953, 2012.
- [12] F. Schwierz, "Electronics: Industry-compatible graphene transistors," *Nature*, vol. 472, no. 7341, pp. 41–42, 2011.

- [13] B. N. Szafranek, G. Fiori, D. Schall, D. Neumaier, and H. Kurz, "Current Saturation and Voltage Gain in Bilayer Graphene Field Effect Transistors," *Nano Letters*, vol. 12, no. 3, pp. 1324–1328, 2012.
- [14] G. Fiori and G. Iannaccone, "Insights on radio frequency bilayer graphene FETs," in *Electron Devices Meeting (IEDM), 2012 IEEE International*, 2012, pp. 17.3.1–17.3.4.
- [15] Y. Wu, D. B. Farmer, W. Zhu, S.-J. Han, C. D. Dimitrakopoulos, A. A. Bol, P. Avouris, and Y.-M. Lin, "Three-Terminal Graphene Negative Differential Resistance Devices," *ACS Nano*, vol. 6, no. 3, pp. 2610–2616, 2012.
- [16] S.-J. Han, D. Reddy, G. D. Carpenter, A. D. Franklin, and K. A. Jenkins, "Current saturation in submicrometer graphene transistors with thin gate dielectric: Experiment, simulation, and theory," *ACS Nano*, vol. 6, no. 6, pp. 5220–5226, 2012.
- [17] D. Dragoman and M. Dragoman, "Negative differential resistance of electrons in graphene barrier," *Appl. Phys. Lett.*, vol. 90, no. 14, p. 143111, 2007.
- [18] V. N. Do, V. H. Nguyen, P. Dollfus, and A. Bournel, "Electronic transport and spin-polarization effects of relativisticlike particles in mesoscopic graphene structures," *J. Appl. Phys.*, vol. 104, no. 6, p. 063708, 2008.
- [19] P. Zhao, Q. Zhang, D. Jena, and S. O. Koswatta, "Influence of Metal-Graphene Contact on the Operation and Scalability of Graphene Field-Effect Transistors," *IEEE Trans. Electron Devices*, vol. 58, no. 9, pp. 3170–3178, 2011.
- [20] R. Grassi, T. Low, A. Gnudi, and G. Baccarani, "Contact-Induced Negative Differential Resistance in Short-Channel Graphene FETs," *IEEE Trans. Electron Devices*, vol. 60, no. 1, pp. 140–146, 2013.
- [21] A. Alarcon, V.-H. Nguyen, S. Berrada, D. Querlioz, J. Saint-Martin, A. Bournel, and P. Dollfus, "Pseudosaturation and Negative Differential Conductance in Graphene Field-Effect Transistors," *IEEE Trans. Electron Devices*, vol. 60, no. 3, pp. 985–991, 2013.
- [22] K. Ganapathi, Y. Yoon, M. Lundstrom, and S. Salahuddin, "Ballistic $I - V$ Characteristics of Short-Channel Graphene Field-Effect Transistors: Analysis and Optimization for Analog and RF Applications," *IEEE Trans. Electron Devices*, vol. 60, no. 3, pp. 958–964, 2013.
- [23] Y. Tsididis, *Operation and modeling of the MOS transistor*, 2nd ed. Boston, MA: McGraw-Hill, 1999.
- [24] S. Datta, *Quantum Transport: Atom to Transistor*. Cambridge, UK: Cambridge University Press, 2005.
- [25] K. D. Holland, N. Paydavosi, N. Neophytou, D. Kienle, and M. Vaidyanathan, "RF Performance Limits and Operating Physics Arising From the Lack of a Bandgap in Graphene Transistors," *IEEE Trans. Nanotechnol.*, vol. 12, no. 4, pp. 566–577, 2013.
- [26] S. O. Koswatta, A. Valdes-Garcia, M. B. Steiner, Y.-M. Lin, and P. Avouris, "Ultimate RF performance potential of carbon electronics," *IEEE Trans. Microw. Theory Tech.*, vol. 59, no. 10, pp. 2739–2750, 2011.
- [27] I. Meric, M. Y. Han, A. F. Young, B. Ozyilmaz, P. Kim, and K. L. Shepard, "Current saturation in zero-bandgap, top-gated graphene field-effect transistors," *Nature Nanotechnology*, vol. 3, pp. 654–659, 2008.
- [28] T. Low, S. Hong, J. Appenzeller, S. Datta, and M. S. Lundstrom, "Conductance Asymmetry of Graphene p-n Junction," *IEEE Trans. Electron Devices*, vol. 56, no. 6, pp. 1292–1299, 2009.
- [29] Y.-M. Lin, H.-Y. Chiu, K. Jenkins, D. B. Farmer, P. Avouris, and A. Valdes-Garcia, "Dual-Gate Graphene FETs With f_T of 50 GHz," vol. 31, no. 1, pp. 68–70, 2010.
- [30] W. Zhu, T. Low, D. B. Farmer, K. Jenkins, B. Ek, and P. Avouris, "Effect of dual gate control on the alternating current performance of graphene radio frequency device," *Journal of Applied Physics*, vol. 114, no. 4, p. 044307, 2013.
- [31] W. H. Press, B. P. Flannery, S. A. Teukolsky, and W. T. Vetterling, *Numerical recipes in C: the art of scientific computing*, 2nd ed. Cambridge: Cambridge Univ. Press, 1992.
- [32] D. M. Pozar, *Microwave engineering*, 3rd ed. Hoboken, NJ: Wiley, 2005.
- [33] J. S. Moon, M. Antcliffe, H. C. Seo, D. Curtis, S. Lin, A. Schmitz, I. Milosavljevic, A. A. Kiselev, R. S. Ross, D. K. Gaskill, P. M. Campbell, R. C. Fitch, K.-M. Lee, and P. Asbeck, "Ultra-low resistance ohmic contacts in graphene field effect transistors," *Applied Physics Letters*, vol. 100, no. 20, p. 203512, 2012.
- [34] Z. Guo, R. Dong, P. S. Chakraborty, N. Lourenco, J. Palmer, Y. Hu, M. Ruan, J. Hankinson, J. Kunc, J. D. Cressler, C. Berger, and W. A. de Heer, "Record maximum oscillation frequency in c-face epitaxial graphene transistors," *Nano Letters*, vol. 13, no. 3, pp. 942–947, 2013.
- [35] F. Schwier, "Graphene Transistors: Status, Prospects, and Problems," *Proc. IEEE*, vol. 101, no. 7, pp. 1567–1584, 2013.
- [36] F. Traversi, V. Russo, and R. Sordan, "Integrated complementary graphene inverter," *Appl. Phys. Lett.*, vol. 94, no. 22, p. 223312, 2009.
- [37] H.-Y. Chen and J. Appenzeller, "On the voltage gain of complementary graphene voltage amplifiers with optimized doping," vol. 33, no. 10, pp. 1462–1464, 2012.